Pb^{2+}-stabilized Ruddlesden–Popper $(Sr_{1-x}Pb_x)_3Ti_2O_7$ ceramics

Feng Gao
Department of Materials Science and Engineering, Pennsylvania State University, PA 16802, USA; and State Key Laboratory of Solidification Processing, School of Material Science and Engineering, Northwestern Polytechnical University, Xi'an, Shaanxi 710072, China

Yunfei Chang
Department of Materials Science and Engineering, Pennsylvania State University, PA 16802, USA; and Condensed Matter Science and Technology Institute & School of Science, Harbin Institute of Technology, Harbin 150080, Heilongjiang, China

Stephen F. Poterala, Elizabeth Kupp, and Gary L. Messing[a),b)]
Department of Materials Science and Engineering, Pennsylvania State University, PA 16802, USA

(Received 7 January 2016; accepted 5 April 2016)

Pb^{2+}-doped $(Sr_{1-x}Pb_x)_3Ti_2O_7$ (SPT) ceramics were fabricated by a solid state reaction. The stability and lattice structure of $Sr_3Ti_2O_7$ and $Sr_4Ti_3O_{10}$ Ruddlesden–Popper (RP) phases were studied as a function of Pb^{2+} content and sintering atmosphere. X-ray diffraction indicates that $SrO(SrTiO_3)_n$ RP phase formation is sensitive to the Sr:Ti ratio of the raw materials and is a complex circularly iterative process. When the PbO concentration is less than $x = 0.03$, pure $Sr_3Ti_2O_7$ can be obtained. $Sr_4Ti_3O_{10}$ was found to be the main phase in the SPT samples for $x \geq 0.075$. Pb^{2+} stabilizes $SrO(SrTiO_3)_n$ RP phases by substitution for Sr^{2+} which reduces the lattice stress of the RP phase. It was observed that SrO vaporization losses at high temperature can be compensated by the decomposition of the intermediate $SrPbO_3$ phase at lower temperature.

I. INTRODUCTION

Direct conversion between thermal and electrical energy using thermoelectric (TE) materials may have important social benefits for energy efficiency.[1,2] As with many technologies, however, the TE materials themselves limit the device performance. Enhancement of TE properties can be achieved by lowering the thermal conductivity (k) while avoiding significant deterioration of the Seebeck coefficient (S) and the electrical conductivity (σ). One way to achieve this enhancement is to engineer the superlattice structure.[3,4]

Ruddlesden–Popper (RP)-type $SrO(SrTiO_3)_n$ phases show great potential for realization of low k owing to their superlattice structure.[5–7] $SrO(SrTiO_3)_n$ is a superlattice of SrO layers and $SrTiO_3$ slabs alternately stacked along the c-axis. As with engineered superlattices, such natural superlattices can be expected to show significant anisotropy in thermal transport, with the thermal conductivity through the layers along the c-axis being significantly lower than within the layers. The interfaces between SrO layers and $SrTiO_3$ slabs may enhance phonon scattering and lead to a lower thermal conductivity.[8]

McCoy et al. reported that $Sr_3Ti_2O_7$ (S3T) and $SrTiO_3$ are the only stable $SrO(SrTiO_3)_n$ phases.[9] Most of the literature focuses on synthesizing platelet-shaped S3T particles by the molten salt synthesis (MSS) method.[10,11] Although S3T particles with plate-like morphology can be easily prepared using MSS and S3T thin films can be grown epitaxially on $SrTiO_3$ substrates,[12,13] it is difficult to prepare either single crystals or bulk ceramics of phase pure S3T due to complex decomposition reactions.[14] Koumoto's group reported the properties of rare-earth ion (La, Nd, Sm, and Gd)-doped and Nb-doped S3T TE materials synthesized by calcining the powder twice at 1400–1450 °C in Ar, followed by hot pressing at 1400–1450 °C in Ar.[15,16] Detailed information about the relationship between phase structure and process parameters was not presented, and this long, complex fabrication procedure was expensive and hard to control. Until now, the reasons for the decomposition and phase transition of the RP phase have not been well understood. Furthermore, little work has focused on the fabrication of phase pure S3T bulk ceramics under normal sintering conditions, or the mechanism of the stabilization of the S3T RP phase using dopant ions.

Lead (Pb) has been widely used in traditional metal or semiconductor TE materials for its high effective mass.[17,18] Since the ionic radius of Pb^{2+} (119 pm) is similar to that of Sr^{2+} (118 pm) and Pb^{2+} has the same valence as Sr^{2+}, PbO is a good candidate for stabilizing

Contributing Editor: Scott T. Misture
[a)]Address all correspondence to this author.
e-mail: messing@ems.psu.edu
[b)]This author was an editor of this journal during the review and decision stage. For the *JMR* policy on review and publication of manuscripts authored by editors, please refer to http://www.mrs.org/jmr-editor-manuscripts/.
A previous error in this article has been corrected, see 10.1557/jmr.2016.202.
DOI: 10.1557/jmr.2016.164

 © Materials Research Society 2016

https://doi.org/10.1557/jmr.2016.164 Published online by Cambridge University Press

the $SrO(SrTiO_3)_n$ RP phase. In addition, the replacement of Pb^{2+} for Sr^{2+} can also increase the effective carrier mass, which should be beneficial for reducing the thermal conductivity of TE materials.

In this study, we investigated the stability of the S3T RP phase as a function of Pb^{2+} concentration. To understand the stabilization mechanism, the lattice characteristics such as bond lengths and bond angles were studied in detail for both S3T and $Sr_4Ti_3O_{10}$ RP phases. We believe that the determination of the stabilization mechanism of the $SrO(SrTiO_3)_n$ RP phase is useful for developing an effective procedure for fabricating phase pure S3T by a conventional solid state method.

II. EXPERIMENTAL PROCEDURE

Strontium titanate samples were prepared by solid-state reaction using stoichiometric amounts of $SrCO_3$ (99.9%, Alfa Aesar), TiO_2 (99.5%, Rutile grade, Alfa Aesar), and PbO (99.9%, Alfa Aesar). The general formula of the material studied is $(Sr_{1-x}Pb_x)_3Ti_2O_7$ (designated as SPT), where x is 0, 0.01, 0.03, 0.05, 0.075, 0.1, and 0.125. The compositions and sample identification are shown in Table I. The initial stoichiometric compositions were ball-milled with ZrO_2 media in ethanol for 16 h. After drying in an oven at 70 °C for 24 h, the powder mixture was calcined at 1150 °C for 4 h, and then ball milled with 6 mm diameter ZrO_2 media for 24 h. The milled powders were pressed into disks of 1 mm thickness and 12.7 mm diameter at 200 MPa, and then sintered at 1400–1550 °C for 2 h in air. SPT samples were also sintered in Ar and O_2 to further investigate the influence of atmosphere on the phase formation.

Sample densities were measured using the Archimedes method. The theoretical density of the mixed phase samples was calculated from the fraction of phases obtained by Rietveld refinement. The phase structure and lattice constants were examined by x-ray diffraction (XRD, PANalytical, Inc. Xpert Pro MPD diffractometer, Holland) using Cu K_α radiation with a step size of 0.02°. Crystallographic data were obtained using Rietveld analysis and JADE 9.0 software. The quality of the refinement was quantified by the corresponding figures of merit: weighted profile residual R_{wp} and goodness of fit indicator $S = R_{wp}/R_{exp}$. For SPT-01~SPT-125 samples, R_{wp} is in the range of 11.94–14.79%, S is in the range of 1.26–1.84. We believe that the Rietveld analysis shows a reasonable fit.

Thermally-etched microstructures were observed by scanning electron microscopy (SEM; Hitachi S-3500, Hitachi Corp., Tokyo, Japan).

TABLE I. Composition and identification of SPT samples.

Sample ID	SPT
S3T	S3T
SPT-01	$(Sr_{0.99}Pb_{0.01})_3Ti_2O_7$
SPT-03	$(Sr_{0.97}Pb_{0.03})_3Ti_2O_7$
SPT-05	$(Sr_{0.95}Pb_{0.05})_3Ti_2O_7$
SPT-075	$(Sr_{0.925}Pb_{0.075})_3Ti_2O_7$
SPT-10	$(Sr_{0.90}Pb_{0.10})_3Ti_2O_7$
SPT-125	$(Sr_{0.875}Pb_{0.125})_3Ti_2O_7$

III. RESULTS AND DISCUSSION

A. Characteristics of undoped S3T samples

Figure 1 shows XRD patterns of calcined and sintered undoped S3T samples. As evidenced by peaks at 2θ = 31.806° and 44.505°, which correspond to the (105) and (0010) planes, respectively, S3T was obtained by calcining a mixture of $SrCO_3$ and TiO_2 at 1150 °C for 4 h. After S3T samples were sintered, the (105) peak becomes weaker and the (0010) peak disappears. It is obvious that S3T and $SrTiO_3$ coexist and $SrTiO_3$ is the main phase in the samples sintered at 1450–1550 °C. The amount of $SrTiO_3$ phase increases with increasing sintering temperature.

The relative densities and phase contents of S3T ceramics sintered at different temperatures are shown in Table II. The S3T samples were <86% dense even after sintering to a temperature as high as 1550 °C. The weight of the samples decreases with increasing sintering temperature, as a result of SrO evaporation. Evaporation is supported by the fracture surface of the sample sintered at 1550 °C (Fig. 2) which shows the formation of ≥20 μm pores and increased weight losses of 4.9 and 6.9% when sintered at 1450 and 1550 °C, respectively. Based on these initial studies, we believe that S3T decomposes to form $SrTiO_3$ due to the evaporation of SrO, as shown in Eq. (1).

$$Sr_3TiO_3O_7 \rightarrow 2SrTiO_3 + SrO\uparrow \quad . \qquad (1)$$

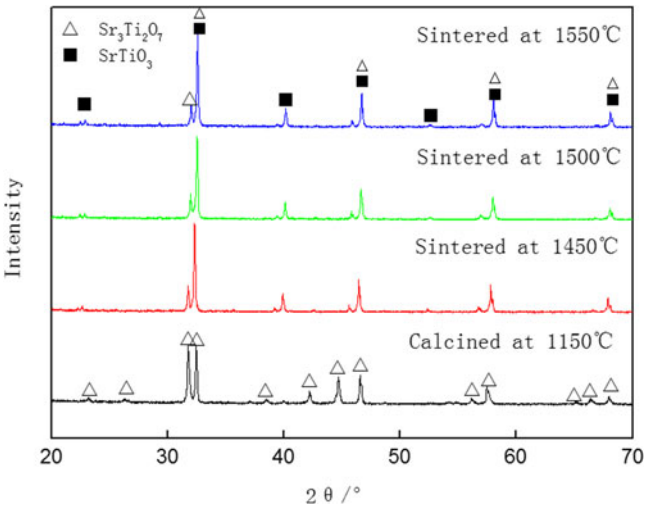


FIG. 1. XRD patterns of undoped S3T (SPT) samples calcined at 1150 °C for 4 h and air-sintered at different temperatures.

https://doi.org/10.1557/jmr.2016.164 Published online by Cambridge University Press

TABLE II. Phase compositions and densities of air sintered S3T samples.

T/°C	Content of $SrTiO_3$/%	Content of S3T/%	Density/ g·cm^{-3}	Relative density/%	Weight loss/%
1450	75.9	24.1	4.12	80.65	4.90
1500	76.1	23.9	4.25	83.19	6.17
1550	83.2	16.8	4.37	85.51	6.89

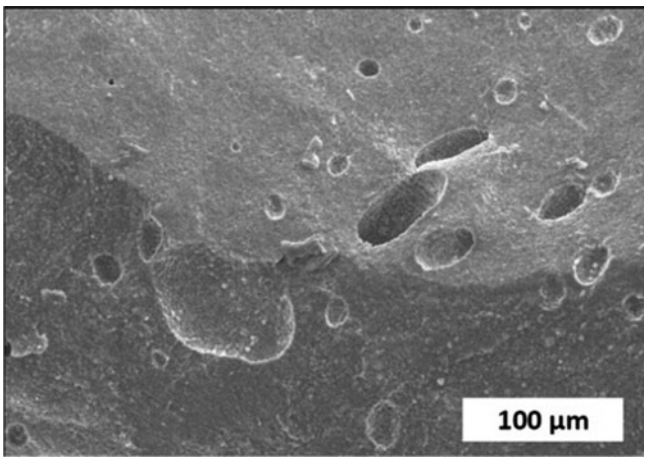


FIG. 2. SEM micrograph of an S3T sample sintered at 1550 °C for 2 h in air showing large pores due to SrO evaporation.

$SrTiO_3$ can also be regarded as a kind of $SrO(SrTiO_3)_n$ RP phase with $n = \infty$ and is the most stable compound in the Sr–Ti–O RP system. In a $SrTiO_3$ unit cell, the coordination number of Sr^{2+} is 12, and that of Ti^{4+} is 6. The bond lengths and bond angles of Sr–O and Ti–O are shown in Table SI (see supplementary material). $SrTiO_3$ has the strongest 3-dimensional stability in the SrO–($SrTiO_3$) system since all of the Ti–O bonds have the same bond length (0.1952 nm) with bond angles of 90°. The same characteristics can be found for the Sr–O bond, as shown in Fig. SI(a) and Table SI.

The unit cell of S3T consists of defect layers of SrO between sheets of $SrTiO_3$ perovskite layers. These planar defects can be described by removal of the sheets of TiO_6 octahedra along (001) and shear of the remaining perovskite layers by 1/2[111].[19,20] In the S3T crystal structure, the Sr^{2+} cation has two different positions in the lattice—one with a coordination number of 12 (labeled Sr_1), which is located in the octahedra stack, and one with the coordination number of 9 (labeled Sr_2), located at the boundary between the octahedra stack and the rock salt SrO layer, as shown in Fig. SI(b) (see supplementary material). This analysis indicates that the S3T crystal structure can accept two different cations at the Sr^{2+} positions and that the Sr_1 position can be filled with larger cations.[21]

The crystallographic data of calcined S3T were analyzed by Rietveld refinement based on the *I*4/*mmm* space group. The Rietveld fitting of S3T is shown in Fig. SII (see supplementary material). The reliability factor *R* was 11.99%, indicating a reasonable fit. The calculated crystal parameters such as bond lengths and bond angles are given in Table SII (see supplementary material). In agreement with the standard crystallographic data of the $SrTiO_3$ lattice structure, bond lengths of Ti–O_1 and Ti–O_2 are almost the same (0.1951 and 0.1952 nm) and the bond angles O_i–Ti–O_j ($i \neq j$, $i, j = 1, 2, 3$) were 90°. The Ti–O_3 bond length was shorter (0.1933 nm). This result indicates that the Ti–O octahedra were maintained in the perovskite layer of the S3T lattice structure. However, the main difference was found in the Sr–O bond lengths and angles. All of the Sr–O bond lengths are shorter in S3T than in the $SrTiO_3$ cell, and the Sr–O bond angles were distorted from −4.22° to 2.06°. These data demonstrate an asymmetric structure which contributes to the metastability of the S3T structure.

The bond length of Sr_2–O_2 is important, because the Sr_2–O_2 bonds connect the rock-salt SrO and the perovskite layers. The Sr_2–O_2 bond length is the shortest (0.2544 nm) of the Sr–O bonds. The percent change in the Sr_2–O_2 bond length amounts to −7.86% which is a large change from the equilibrium position and thus significant stress must be generated in the lattice. As a result, the entire S3T lattice lies in a relatively high energy state and the Sr_2–O_2 bonds are easily broken by lattice vibrations at high temperatures, releasing the lattice stress. Finally, breaking the Sr_2–O_2 bond leads to the phase transformation from S3T to $SrTiO_3$ and a new equilibrium is established. This analysis demonstrates why it is difficult to prepare SPT ceramics using conventional sintering but suggests that S3T can be stabilized by chemical substitution which alleviates these lattice stresses.

B. Characteristics of SPT samples sintered in air

Figure 3 shows XRD patterns of SPT powders calcined at 1150 °C for 4 h. It reveals that phase pure S3T was obtained when PbO is doped at an amount less than $x = 0.075$. The characteristic peaks (105) and (0010) can be clearly distinguished. When the PbO amount is higher than $x = 0.05$, $SrPbO_3$ begins to appear in addition to the $SrTiO_3$ phase. $SrTiO_3$, S3T, and $SrPbO_3$ coexist in the calcined SPT samples when heated from 1450 °C to 1550 °C. The percentage of each phase in the calcined powders is listed in Table III. It can be seen that the concentration of $SrPbO_3$ and $SrTiO_3$ increase with increasing PbO concentrations. Although PbO evaporates at 889 °C, due to its low melting point, it appears that PbO reacts with $SrCO_3$ to form $SrPbO_3$. Moreover, the Sr:Ti ratios of SPT-10 and SPT-125 samples are much closer to that of $Sr_4Ti_3O_{10}$, but $Sr_4Ti_3O_{10}$ was not observed in the calcined powders further demonstrating that Pb^{2+} stabilizes S3T.

https://doi.org/10.1557/jmr.2016.164 Published online by Cambridge University Press

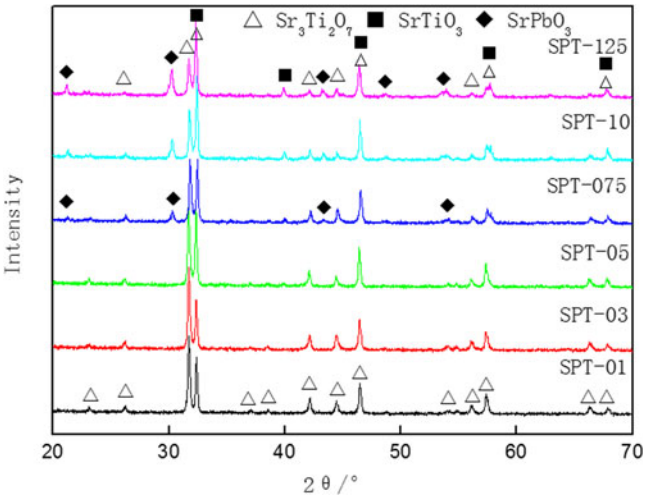


FIG. 3. XRD patterns of SPT powders air calcined at 1150 °C for 4 h.

TABLE III. Phase composition of SPT samples calcined at 1150 °C for 4 h and then air-sintered at 1550 °C for 2 h.

	Calcined powders			Sintered ceramics	
Samples	$SrTiO_3$/%	S3T/%	$SrPbO_3$/%	S3T/%	$Sr_4Ti_3O_{10}$/%
SPT-01	...	100	...	100	...
SPT-03	...	100	...	80.4	19.6
SPT-05	9.5	88.3	2.2	62.5	37.5
SPT-075	15.4	81	3.6	31.8	68.2
SPT-10	31.4	61.5	7.1	12.4	87.6
SPT-125	39.1	49.9	11.0	9.7	90.3

XRD patterns for the SPT samples sintered at 1550 °C in air are shown in Fig. 4. Pure S3T is obtained in the SPT-01 sample. It is interesting to note that the $SrTiO_3$ and $SrPbO_3$ phases in the calcined powder are not present in the sintered samples. Although the most intense peak is still at $2\theta \approx 31.8°$, i.e., the (105) plane of S3T, further analysis shows that the peak can be divided into two peaks, one belonging to the (105) plane of the S3T phase, and the other to the (107) plane of the $Sr_4Ti_3O_{10}$ phase, as shown in Fig. 4(b). $Sr_4Ti_3O_{10}$ and S3T coexist in all of the sintered samples except SPT-01.

The concentrations of the $Sr_4Ti_3O_{10}$ and S3T phases in the sintered samples, as determined by Rietveld refinement of the XRD patterns, are listed in Table III. It is clear that the concentration of S3T phase decreases with increasing PbO, whereas the concentration of $Sr_4Ti_3O_{10}$ increases. When the PbO dopant is less than $x = 0.05$, S3T is the major phase (i.e., its concentration is above 50%). When the PbO doping level is higher than 0.075, $Sr_4Ti_3O_{10}$ is the major phase and it reaches a maximum of 90.3% when $x = 0.25$.

The lattice constants of the S3T phase in the samples with $x = 0$–0.075 were calculated and the variation of lattice constant with increasing PbO content is plotted in Fig. 5. It is seen that both the *a* and *c* parameters increase with increasing PbO content, which results in a larger lattice volume. In addition, the *c*/*a* ratio decreases, suggesting that the degree of tetragonality is reduced. To further understand the mechanism of the Pb^{2+} substitution, the formation enthalpy of the Pb-doped S3T is calculated by the first principle theory, as shown in Table SIII (see supplementary material). The calculated results demonstrate that the unit cell of Pb^{2+}-doped S3T has a relatively lower energy. Thus, doping with a small concentration of Pb can improve the structural stability, and the structure's thermodynamic stability is better when Pb^{2+} substitutes for Sr^{2+} at Sr_1 positions in the RP lattice structure. This substitution leads to distortion of the lattice and contributes to the slight increase of the lattice constants *a* and *c*.

Based on the XRD results of the calcined powders, we consider two phenomena; one is the disappearance of the $SrPbO_3$ phase, and the other is the formation of $Sr_4Ti_3O_{10}$ phase. It is easy to understand why the $SrPbO_3$ phase disappears since $SrPbO_3$ transforms from orthorhombic to tetragonal at ~450 °C, and subsequently transforms from tetragonal to cubic at ~810 °C. Finally, $SrPbO_3$ decomposes to SrO and PbO above 1000 °C, as shown in the following formula.[22,23]

$$SrPbO_3 \xrightarrow{\geq 1000^{\circ}C} PbO\uparrow + SrO\uparrow + \frac{1}{2}O_2\uparrow \quad . \qquad (2)$$

The formation of $Sr_4Ti_3O_{10}$ is most sensitive to the original Sr:Ti ratio. Because the Sr:Ti ratios of SPT-075, SPT-10, and SPT-125 are much closer to that of $Sr_4Ti_3O_{10}$, $Sr_4Ti_3O_{10}$ is the major phase in the sintered ceramics.

$Sr_4Ti_3O_{10}$ is an intermediate phase between $SrTiO_3$ and S3T. $Sr_4Ti_3O_{10}$ has a tetragonal structure with the space group of *I4/mmm* and lattice parameters of $a = 0.39$ nm, $c = 2.81$ nm (PDF No. 97-003-4630). The lattice structure of $Sr_4Ti_3O_{10}$ is more complex than that of S3T since the Sr^{2+} cation has three different positions in the unit cell. The additional position for the Sr^{2+} with a coordination number of 12 is located in the middle of the octahedral layer, labeled Sr_3, as shown in Fig. SIII (see supplementary material). In addition, there are two different positions for Ti^{4+} cations. One is located in the center layer of the three TiO_6 octahedral layers (Ti_1), and the other is in the oxygen octahedral position close to the edge of the rock-salt SrO layers (Ti_2). Rietveld refinement of the $Sr_4Ti_3O_{10}$ lattice structure shows that all of the Sr–O bond lengths are shorter than those in the $SrTiO_3$ cell, and the Sr–O bond angles are distorted, similar to the characteristics observed in S3T. The perovskite layer in $Sr_4Ti_3O_{10}$ does not have cubic symmetry.

https://doi.org/10.1557/jmr.2016.164 Published online by Cambridge University Press

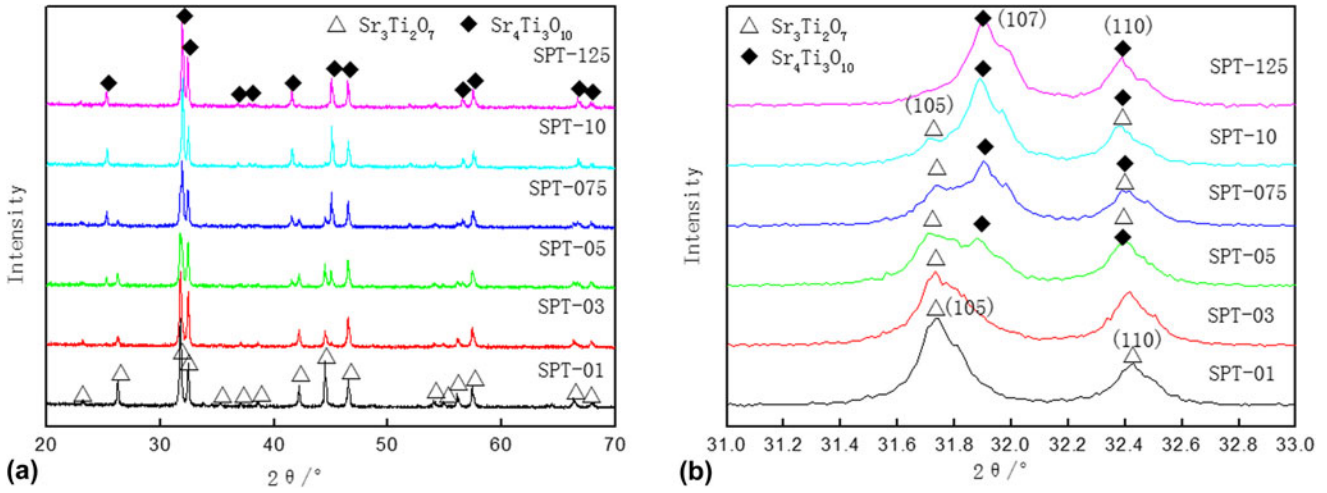


FIG. 4. XRD patterns of SPT samples air sintered at 1550 °C for 2 h, (a) 2θ = 20–70° and (b) 2θ = 31–33°.

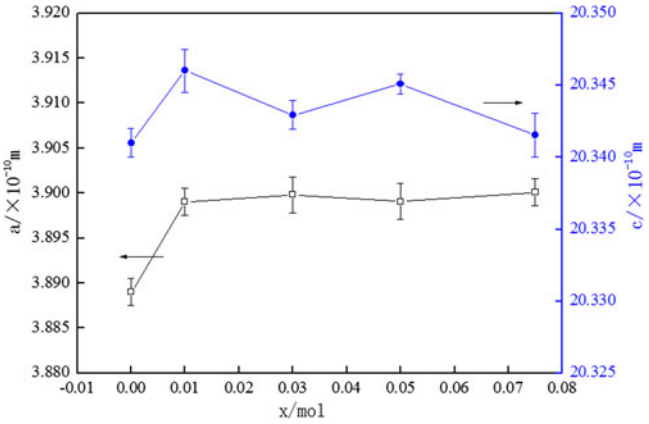


FIG. 5. Lattice constants of S3T in the SPT samples sintered at 1550 °C in air.

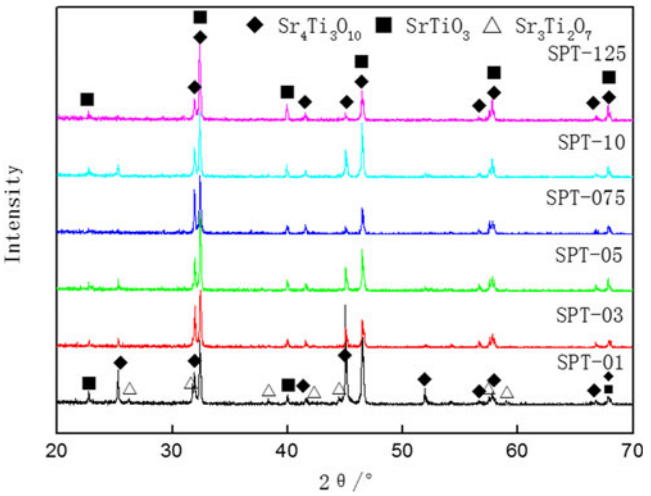


FIG. 6. XRD patterns of SPT samples sintered at 1550 °C in Ar.

The $Sr_4Ti_3O_{10}$ crystal structure can be characterized by four parameters (D1, D2, D3, and S1) along the *c*-axis, which represent the different Ti–O distances inside the TiO_6 octahedra, and the Sr_2–O_2 interplanar distance, respectively, as indicated in Fig. SIII. It should be noted that the structure refinement performed by RP assumed no rumpling and that all of the Ti–O bonds along the *c*-axes have the same length.[24,25] In reality, the Ti–O bond lengths are not all the same. D1, D2, and D3 are 0.1911 nm, 0.1855 nm, and 0.1967 nm, respectively. This implies the presence of deformed TiO_6 octahedra. The largest change in the Ti–O bond length amounts to −4.97%, compared to the stable Ti–O bond length (0.1952 nm) in $SrTiO_3$. The Sr_2–O_2 bond length (S1) between the TiO_6 octahedra and the SrO layers is still the shortest one, pushing the oxygen and strontium atoms away from and towards the TiO_6 octahedra layers, respectively. This result reveals that the $Sr_4Ti_3O_{10}$ crystal structure stays in a much higher energy state and is even more unstable than S3T.

Several papers report that S3T is the most stable phase among the RP compounds in the $SrO(SrTiO_3)_n$ system and that there is no driving force to form single-phase samples with higher *n*.[26,27] However, the $Sr_4Ti_3O_{10}$ phase is found to be the main phase in the SPT samples with $x \geq 0.075$. To determine whether Pb^{2+} stabilizes $Sr_4Ti_3O_{10}$ by alleviating lattice strain, crystallographic data for $Sr_4Ti_3O_{10}$ (JCPDF data PDF No. 97-003-4630) and SPT-125 by Rietveld refinement are shown in Table SIV (see supplementary material). Expansion of both the *a*-axis and the *c*-axis were observed, resulting in an overall increase of lattice parameters *a* and *c*. It is clear that both the Ti–O and Sr_2–O_2 bond lengths are larger than those in undoped $Sr_4Ti_3O_{10}$. These results indicate that Pb^{2+} can substitute for Sr^{2+} in the $Sr_4Ti_3O_{10}$ lattice and increase the Ti–O and Sr_2–O_2 bond lengths. It is believed that this substitution decreases the lattice stress, causing the lattice to shift to a relatively lower energy state and aid in the stabilization of $Sr_4Ti_3O_{10}$.

https://doi.org/10.1557/jmr.2016.164 Published online by Cambridge University Press

TABLE IV. Effect of atmosphere on phase compositions of SPT samples sintered at 1550 °C.

	Sintered in Ar			Sintered in O_2		
Samples	$SrTiO_3$/%	S3T/%	$Sr_4Ti_3O_{10}$/%	$SrTiO_3$/%	S3T/%	$Sr_4Ti_3O_{10}$/%
SPT-01	39.2	15.1	45.7	16.8	30.2	53
SPT-03	43	0	57	19.9	17.3	62.8
SPT-05	50	0	50	...	...	...
SPT-075	45.8	0	54.2	10.2	21.6	68.2
SPT-10	48.9	0	51.1	...	...	...
SPT-125	66.5	0	33.5	35.5	0	64.5

In addition to the effect of Pb^{2+} on the stabilization of the RP lattice structure, the function of SrO on the formation of the RP phase should also be considered. During sintering, the final phase structure comes from a series of complex, iterative reactions, described as the following equations:

$$2SrTiO_3 + SrO \rightarrow Sr_3Ti_2O_7 \quad , \tag{3}$$

$$3SrTiO_3 + SrO \rightarrow Sr_4Ti_3O_{10} \quad , \tag{4}$$

$$Sr_3Ti_2O_7 + SrTiO_3 \rightarrow Sr_4Ti_3O_{10} \quad . \tag{5}$$

It was demonstrated that $SrTiO_3$ is present in the final product if there is insufficient SrO during sintering. SrO is highly reactive and can easily react with atmospheric H_2O and CO_2. The direct addition of excess SrO to the raw materials does not enhance RP phase formation because SrO evaporates before it can react at high temperatures. However, SrO can be introduced at higher temperatures in the form of $SrPbO_3$ and thus participate in the reactions in Eqs. (3) and (4) to form SPT.

Generally, PbO doping is beneficial for stabilizing the S3T and $Sr_4Ti_3O_{10}$ RP phases. The final phase structure, either S3T or $Sr_4Ti_3O_{10}$, is sensitive to the Sr:Ti ratio of the raw materials, which means that only the SPT-01 sample resulted in phase pure S3T. To ensure the initial Sr:Ti ratio of the RP phase, adding "excess" PbO is more effective than doping "stoichiometrically".

C. Effect of atmosphere on the characteristics of sintered SPT samples

Since most of the oxide TE materials should be semiconducting under reducing atmospheres, it is necessary to investigate the characteristics of SPT samples sintered under different atmospheric conditions. Figure 6 shows XRD patterns of the SPT samples sintered in Ar at 1550 °C. It is interesting that only S3T exits in the $(Sr_{0.99}Pb_{0.01})_3Ti_2O_7$ composition (SPT-01), whereas $Sr_4Ti_3O_{10}$ and $SrTiO_3$ phases coexist in the rest of samples (Table IV).

SPT samples sintered in air show a light brown color, while the samples sintered in argon are yellow and have much lower densities than those samples sintered in air. Most of the relative densities are less than 87% (Table V). Even when phase pure S3T was obtained in the calcined SPT-01 and SPT-03 powders, S3T phase was not stable through sintering. The percentage of S3T phase in the SPT-01 sample was 15.1%, which means that most of the S3T phase had transformed to $Sr_4Ti_3O_{10}$ and $SrTiO_3$ phases under the Ar atmosphere.

TABLE V. Effect of atmosphere on relative densities of SPT samples sintered at 1550 °C.

Samples	Sintered in air/%	Sintered in Ar/%	Sintered in O_2/%
SPT-01	93.98	85.18	94.89
SPT-03	94.59	80.99	93.88
SPT-05	95.57	86.76	...
SPT-075	93.72	91.14	93.82
SPT-10	94.06	90.68	...
SPT-125	94.53	86.76	94.31

Another interesting phenomenon is that the center region and the surface of the sintered SPT samples ($x \geq 0.05$) show different colors. For example, the color of the $(Sr_{0.95}Pb_{0.05})_3Ti_2O_7$ (SPT-05) sample changes from gray in center region to light brown, then changes to the yellow on the surface, as shown in Fig. 7(a). Figures 7(b) and 7(c) show the grain morphology of different positions in the SPT-05 sample. It is clear that the sample core has a homogeneous grain structure. There are fewer pores in the core than in the surface region, suggesting a relatively higher density in the core. The surface zone is composed of cubic grains which are interconnected. XRD of powder samples ground from the sintered sample and of the surface region shown in Fig. 8 indicate that two phases, $Sr_4Ti_3O_{10}$ and $SrTiO_3$, co-exist in the powder sample, while only $SrTiO_3$ is observed in the surface region and that the cubic grains are $SrTiO_3$.

Noguera et al. reported that the stability of the SrO $(SrTiO_3)_n$ compounds is associated with phase segregation into $SrTiO_3$ and SrO and with segregation into $SrTiO_3$ and another phase of lower n value, as shown in Eqs. (6) and (7).[25] All segregation energies are very small, with positive values indicating an instability of the $SrO(SrTiO_3)_n$ compound.

https://doi.org/10.1557/jmr.2016.164 Published online by Cambridge University Press

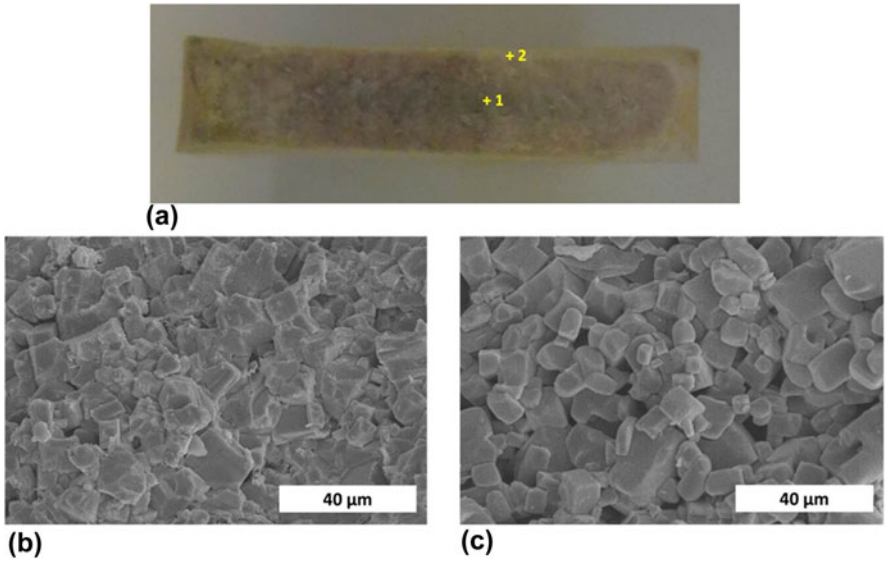


FIG. 7. Microstructure of $(Sr_{0.95}Pb_{0.05})_3Ti_2O_7$ (SPT-05) sample sintered at 1550 °C in Ar, (a) fracture surface, (b) morphology of the sample core (point +1) and (c) morphology of the sample surface (point +2).

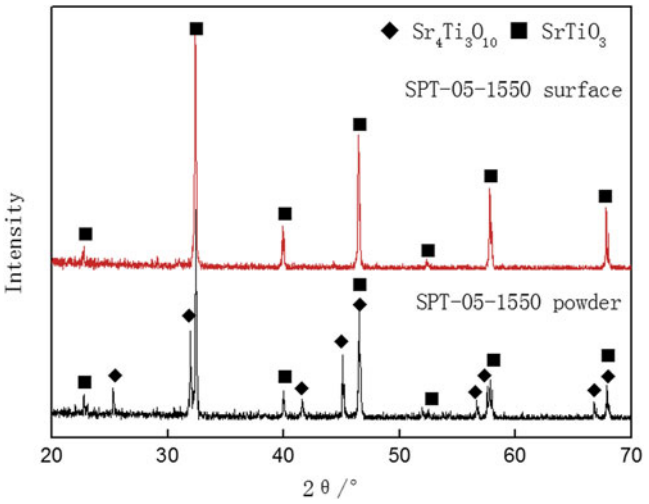


FIG. 8. XRD patterns of $(Sr_{0.95}Pb_{0.05})_3Ti_2O_7$ (SPT-05) samples sintered at 1550 °C in Ar.

$$SrO(SrTiO_3)_n \rightarrow nSrTiO_3 + SrO\uparrow \quad , \qquad (6)$$

$$SrO(SrTiO_3)_n \rightarrow SrO(SrTiO_3)_{n-1} + SrTiO_3 \quad . \qquad (7)$$

According to our experimental results, the phase decomposition of $Sr_4Ti_3O_{10}$ into $SrTiO_3$ and SrO vapor is reasonable, while the transformation from $Sr_4Ti_3O_{10}$ to S3T requires further investigation. Since S3T is one of the most important phases in both the calcined powder and the air-sintered samples, it is believed that SrO vapor is the key to the formation of RP phase. This means that an Ar atmosphere will enhance the transformation from S3T to $SrTiO_3$ and $Sr_4Ti_3O_{10}$, as shown in the following equations:

$$2Sr_3Ti_2O_7 \rightarrow Sr_4Ti_3O_{10} + SrO\uparrow \quad , \qquad (8)$$

$$Sr_4Ti_3O_{10} \rightarrow 3SrTiO_3 + SrO\uparrow \quad , \qquad (9)$$

since flowing Ar enhances decomposition of the RP phase. The decomposition occurs from the sample center towards the surface accompanied with the formation of gaseous SrO. A flowing Ar atmosphere not only lowers the oxygen partial pressure in the furnace, which will produce more oxygen defects in the lattice structure of the RP phase and weaken the bond strength, but also removes gaseous SrO and accelerates the decomposition reaction. This is the reason that the samples have low densities at the surface. It is deduced that the SrO $(SrTiO_3)_n$ RP phase will fully transform to $SrTiO_3$ if the sample is held at elevated temperature for a prolonged time.

McCarthy et al. investigated the phase equilibria of the Sr–Ti–O system and found that an amorphous white powder coated the furnace tube after sintering samples at 1375 °C in air. They supposed the deposit to be pure strontium metal.[28] If this is correct, the following reaction should occur during sintering.

$$Sr_3Ti_2O_7 \xrightarrow{\geq 1300^{\circ}C} 2SrTiO_3 + Sr\uparrow + \frac{1}{2}O_2\uparrow \quad . \qquad (10)$$

Since Strontium (Sr) is a highly reactive metal, it easily reacts with water to produce strontium hydroxide and hydrogen gas, and also burns in air to produce both strontium oxide and strontium nitride.[29] However, we can deduce from the reaction in Eq. (10) that O_2 is generated with the formation of metallic Sr. If the samples were

https://doi.org/10.1557/jmr.2016.164 Published online by Cambridge University Press

sintered under an O_2 atmosphere, the high oxygen partial pressure may reverse the reaction and constrain the decomposition of S3T.

Figure 9 shows XRD patterns of SPT samples sintered in O_2. The results obtained do not support the formation of Sr metal. Both the SPT-01 and SPT-03 samples are composed of $SrTiO_3$, S3T, and $Sr_4Ti_3O_{10}$ phases, with $Sr_4Ti_3O_{10}$ being the major phase. The SPT-125 sample is composed of $SrTiO_3$ and $Sr_4Ti_3O_{10}$ phases, similar to the sample sintered in Ar. The sample densities are much higher than those sintered in Ar, and are almost the same as those sintered in air, as shown in Table V.

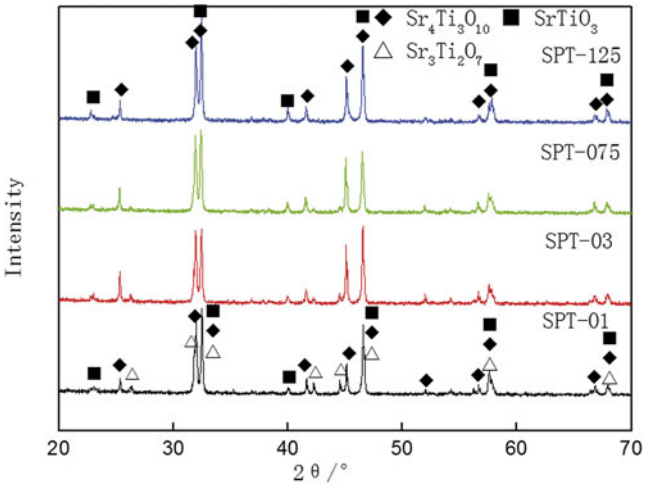


FIG. 9. XRD patterns of SPT samples sintered at 1550 °C in O_2.

Because the SPT-01 sample sintered in air converted to pure S3T, it was chosen as the focus for a discussion on the phase transformation to the RP phase. Figure 10 shows that the microstructures of SPT-01 samples are strongly dependent on the sintering atmosphere. Equiaxed and plate-shape S3T grains coexist in the SPT-01 sample sintered in air, while 10–20 μm cubic $SrTiO_3$ grains are observed in the more porous sample sintered in Ar. The sample sintered in O_2 shows a homogeneously dense microstructure with clear grain boundaries. Some plate-like grains corresponding to the S3T or $Sr_4Ti_3O_{10}$ RP phase can be observed together with the equiaxed $SrTiO_3$ grains.

The results above reveal that O_2 does not constrain the decomposition of S3T during sintering. Compared with the calcined powder, single phase S3T cannot be obtained by sintering in either Ar or O_2. Because flowing Ar and O_2 can remove gaseous SrO from the furnace, sintering under these atmospheres enhances the decomposition of the RP phase. It is believed that the phase transition between the RP phases is a complex reversible process, meaning that $SrO(SrTiO_3)_n$ compounds can phase separate into $SrTiO_3$ and SrO, and $SrO(SrTiO_3)_n$ phases with lower n value, $SrO(SrTiO_3)_{n-1}$, and these phases can react with $SrTiO_3$ to produce $SrO(SrTiO_3)_n$ again. Sintering atmosphere plays an important role in the above phase transformation. However, additional research is needed to understand the effect of atmosphere on low temperature reactions, the reduction in low or no oxygen sintering and the effect of oxygen pressure on the phase transition, the TE properties of the SPT samples, and the

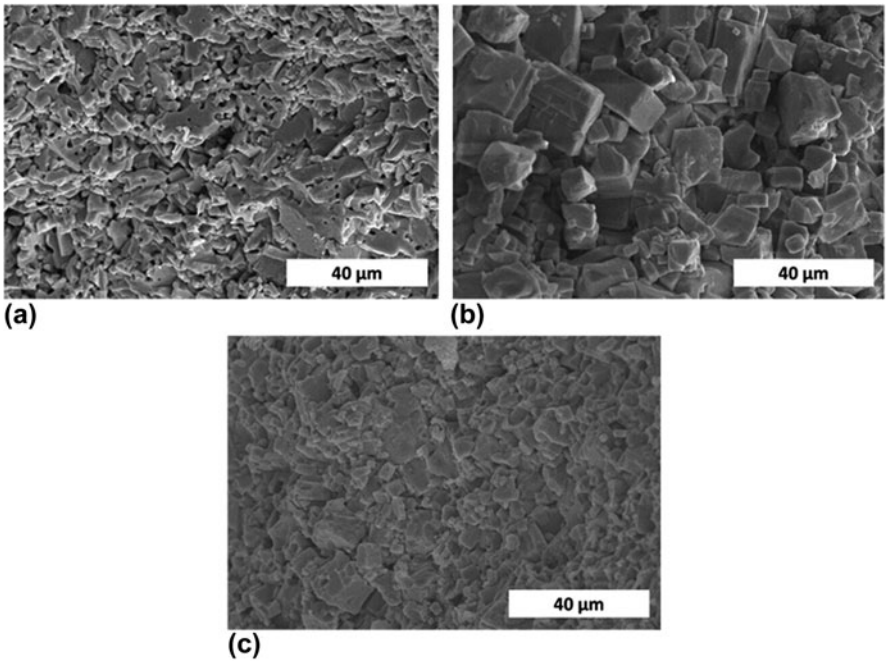


FIG. 10. SEM micrographs of $(Sr_{0.99}Pb_{0.01})_3Ti_2O_7$ (SPT-01) samples sintered in (a) air, (b) Ar, and (c) O_2 at 1550 °C.

https://doi.org/10.1557/jmr.2016.164 Published online by Cambridge University Press

relationship between the $SrO(SrTiO_3)_n$ RP phase composition and its TE properties.

IV. CONCLUSIONS

It is difficult to prepare phase pure S3T ceramics under conventional sintering conditions. Without PbO doping, S3T and $SrTiO_3$ coexist and $SrTiO_3$ is the main phase in the S3T ceramics. Rietveld refinement results show that an asymmetric lattice structure, especially Ti–O and Sr–O bond lengths and angles along the *c*-axis, contribute to the metastability of the S3T and $Sr_4Ti_3O_{10}$ structures. The sintering atmosphere affects the phase transition and the microstructure significantly, with the key to the reactions being control of the evaporation of SrO from the $SrO(SrTiO_3)_n$ phase. Flowing atmospheres of any composition impede sintering by removing volatile species and promoting further decomposition.

The phase transition between the RP phases is a complex circularly iterative process. $SrO(SrTiO_3)_n$ RP phases in SPT samples are more stable than those without Pb^{2+}. When the PbO doping amount x is less than 0.03, pure S3T phase can be obtained. The $Sr_4Ti_3O_{10}$ phase was found to be the main phase in the SPT samples with $x \geq 0.075$. The effect of Pb^{2+} on the phase structure can be described in two ways. On one hand, Pb^{2+} can stabilize $SrO(SrTiO_3)_n$ RP phases through substitution for Sr^{2+} in the lattice, increasing the lattice parameters and decreasing lattice stresses in the RP phase. On the other hand, SrO can be stored in $SrPbO_3$ and survive to higher temperatures. The decomposition of $SrPbO_3$ can compensate for the loss of SrO involved in the RP phase, which enhances the formation of the $SrO(SrTiO_3)_n$ phase.

ACKNOWLEDGMENTS

The author would like to thank Nichole Wonderling from the Materials Characterization Lab in the Materials Research Institute at Penn State for Rietveld refinement discussions. Dr. F. Gao was supported by the Foundation of China Scholarship Council during his stay at The Pennsylvania State University.

REFERENCES

1. R.J. Mehta and G. Ramanath: High efficiency nanobulk thermoelectrics by bottom-up nanocrystal sculpting and assembly. *Am. Ceram. Soc. Bull.* **91**(3), 28 (2012).
2. S. Misture and D. Edwards: High temperature oxide thermoelectrics. *Am. Ceram. Soc. Bull.* **91**(3), 24 (2012).
3. A. Shakouri: Recent developments in semiconductor thermoelectric physics and materials. *Annu. Rev. Mater. Res.* **41**, 399 (2011).
4. S.R.S. Kumar, M.N. Hedhili, D. Cha, T.M. Tritt, and H. N. Alshareef: Thermoelectric properties of strontium titanate superlattices incorporating niobium oxide nanolayers. *Chem. Mater.* **26**, 2726 (2014).
5. A.I. Abutaha, S.R.S. Kumar, K. Li, A.M. Dehkordi, T.M. Tritt, and H.N. Alshareef: Enhanced thermoelectric figure-of-merit in thermally robust, nanostructured superlattices based on $SrTiO_3$. *Chem. Mater.* **27**, 2165 (2015).
6. K. Koumoto, Y.F. Wang, R. Zhang, A. Kosuga, and R. Funahashi: Oxide thermoelectric materials: A nanostructuring approach. *Annu. Rev. Mater. Res.* **40**, 363 (2010).
7. R.R. Sun, X.Y. Qin, L.L. Li, D. Li, J. Zhang, Y.S. Zhang, and C.J. Tang: The effects of elements doping on transport and thermoelectric properties of $Sr_3Ti_2O_7$. *J. Phys. Chem. Solids* **75**, 629 (2014).
8. A. Chernatynskiy, R.W. Grimes, M.A. Zurbuchen, D.R. Clarke, and S.R. Phillpot: Crossover in thermal transport properties of natural, perovskite-structured superlattices. *Appl. Phys. Lett.* **95**, 161906 (2009).
9. M.A. McCoy, R.W. Grimes, and W.E. Lee: Phase stability and interfacial structures in the SrO–$SrTiO_3$ system. *Philos. Mag. A* **75**(3), 833 (1997).
10. Y.F. Liu, Y. Lu, M. Xu, and L.F. Zhoun: Formation mechanisms of platelet $Sr_3Ti_2O_7$ crystals synthesized by the molten salt synthesis method. *J. Am. Ceram. Soc.* **90**(6), 1774 (2007).
11. Y. Ishida, K.I. Kakimoto, H. Ogawa, and M. Aki: Transitional mechanism of particle $Sr_3Ti_2O_7$ morphology in the molten salt synthesis. *Ferroelectrics* **381**, 24 (2009).
12. N.D. Orloff, W. Tian, C.J. Fennie, C.H. Lee, D. Gu, J. Mateu, X.X. Xi, K.M. Rabe, D.G. Schlom, I. Takeuchi, and J.C. Booth: Broadband dielectric spectroscopy of Ruddlesden–Popper $Sr_{n+1}Ti_nO_{3n+1}$ (n = 1, 2, 3. . .) thin films. *Appl. Phys. Lett.* **94**, 042908 (2009).
13. M. Jungbauer, S. Hühn, R. Egoavil, H. Tan, J. Verbeeck, G.V. Tendeloo, and V. Moshnyaga: Atomic layer epitaxy of Ruddlesden–Popper $SrO(SrTiO_3)_n$ films by means of metal-organic aerosol deposition. *Appl. Phys. Lett.* **105**, 251603 (2014).
14. G. Emanuel, A.L. Alexandr, R. Marianne, J. Muller, P. Paufler, and D.C. Meyer: Oriented growth of $Sr_{n+1}Ti_nO_{3n+1}$ Ruddlesden–Popper phases in chemical solution deposited thin films. *J. Solid State Chem.* **179**, 1864 (2006).
15. Y.F. Wang, K.H. Lee, H. Ohta, and K. Koumoto: Thermoelectric properties of electron doped $SrO(SrTiO_3)_n$ (n = 1, 2). *Ceramics. J. Appl. Phys.* **105**, 103701 (2009).
16. K.H. Lee, Y.F. Wang, S.W. Kim, H. Ohta, and K. Koumoto: Thermoelectric properties of Ruddlesden–Popper phase *n*-type semiconducting oxides: La-, Nd-, and Nb-doped $Sr_3Ti_2O_7$. *Int. J. Appl. Ceram. Technol.* **4**(4), 326 (2007).
17. G.J. Snyder and E.S. Toberer: Complex thermoelectric materials. *Nat. Mater.* **7**, 105 (2008).
18. S. Gorsse, P. Bellanger, Y. Brechet, E. Sellier, A. Umarji, U. Ail, and R. Decourt: Nanostructuration via solid state transformation as a strategy for improving the thermoelectric efficiency of PbTe alloys. *Acta Mater.* **59**, 7425 (2011).
19. C.H. Nien and H.Y. Lu: Crystallographic orientation relationships between $SrTiO_3$ and Ruddlesden–Popper phases. *J. Am. Ceram. Soc.* **95**(5), 1676 (2012).
20. A.H. Reshak: Thermoelectric properties of $Sr_{n+1}Ti_nO_{3n+1}$ (n = 1, 2, 3, ∞) Ruddlesdene–Popper homologous series. *Renewable Energy* **76**, 36 (2015).
21. B.V. Beznosikov and K.S. Aleksandrov: Perovskite-like crystals of the Ruddlesden–Popper series. *Crystallogr. Rep.* **45**(5), 792 (2000).
22. K.T. Jacob and K.P. Jayadevan: System Sr–Pb–O: Phase equilibria and thermodynamics using solid-state cells with buffer electrodes. *Chem. Mater.* **12**, 1779 (2000).
23. R. Klein, L.P. Cook, and W. Wong-Ng: Enthalpies of formation of $SrPbO_3$ and Sr_2PbO_4. *J. Chem. Thermodyn.* **34**, 2083 (2002).
24. S.N. Ruddlesden and P. Popper: The compound $Sr_3Ti_2O_7$ and its structure. *Acta Crystallogr.* **11**, 54 (1958).

https://doi.org/10.1557/jmr.2016.164 Published online by Cambridge University Press

25. C. Noguera: Theoretical investigation of the Ruddlesden–Popper compounds $Sr_{n+1}Ti_nO_{3n+1}$ (n = 1–3). *Philos. Mag. Lett.* **80**(3), 173 (2000).
26. S. Kamba, P. Samoukhina, F. Kadlec, J. Pokorny, J. Petzelt, I.M. Reaney, and P.L. Wise: Composition dependence of the lattice vibrations in $Sr_{n+1}Ti_nO_{3n+1}$ Ruddlesden–Popper homologous series. *J. Eur. Ceram. Soc.* **23**, 2639 (2003).
27. K.T. Jacob and G. Rajitha: Thermodynamic properties of strontium titanates: Sr_2TiO_4, $Sr_3Ti_2O_7$, $Sr_4Ti_3O_{10}$, and $SrTiO_3$. *J. Chem. Thermodyn.* **43**, 51 (2011).
28. G.J. Mccarthy, W.B. White, and R. Roy: Phase equilibria in the 1375°C isotherm of the system Sr–Ti–O. *J. Am. Ceram. Soc.* **52**(9), 463 (1969).
29. D.R. Lide: *CRC Handbook of Chemistry and Physics*, 86th ed. (CRC Press, Boca Raton, FL, 2005).

Supplementary Material

To view supplementary material for this article, please visit http://dx.doi.org/10.1557/jmr.2016.164.

https://doi.org/10.1557/jmr.2016.164 Published online by Cambridge University Press